

The autophoretic torus

Lasse C. Schmieding,¹ Eric Lauga,¹ and Thomas D. Montenegro-Johnson^{1,2,*}

¹*Department of Applied Mathematics and Theoretical Physics,
University of Cambridge, Wilberforce Road, Cambridge CB3 0WA, UK.*

²*School of Mathematics, University of Birmingham,
Edgbaston, Birmingham, B15 2TT, UK.*

(Dated: February 7, 2017)

Phoretic swimmers provide new avenues to study non-equilibrium statistical physics and are also hailed as a promising technology for bioengineering at the cellular scale. Exact solutions for the locomotion of such swimmers have been restricted so far to spheroidal shapes. In this paper we solve for the flow induced by the canonical non-simply connected shape, namely an axisymmetric phoretic torus. The analytical solution takes the form of an infinite series solution, which we validate against boundary element computations. For a torus of uniform chemical activity, confinement effects in the hole allow the torus to act as a pump, which we optimize subject to fixed particle surface area. Under the same constraint, we next characterize the fastest swimming Janus torus for a variety of assumptions on the surface chemistry. Perhaps surprisingly, none of the optimal tori occur in the limit where the central hole vanishes.

I. INTRODUCTION

Autophoretic microswimmers are artificial microscale particles that self propel via slip flows at their surface created through self-generated, rather than externally imposed [1, 2], field gradients such as heat [3, 4] or solute concentration [5]. Such particles have potential biomedical [6] and microfluidics applications [7], and may perform intricate microscale tasks, for example directed cargo transport and assembly [8, 9].

In this study, we focus on neutral solute self-diffusiophoresis, in the absence of electrokinetic effects [10, 11], whereby solute chemical reaction differentially catalysed at the swimmer surface leads to local concentration gradients around the swimmer; this property is known as the swimmer’s *activity*. Local pressure imbalances arising from this differential interaction between the particle surface and the solute in a thin layer drive surface slip flows, propelling the swimmer forward; this property is known as the swimmer’s *mobility* [1].

The trajectory of autophoretic microswimmers thus results from the coupled interactions of solute concentration and hydrodynamics, which are in turn strongly influenced by physical conditions such as particle shape [12] and domain boundaries. As such, autophoretic microswimmers exhibit a range of remarkable and complex dynamics, such as self-assembly with neighbouring particles [13] into “living crystals” [14] or rotors and swimmers [15], phase separation [16], swarming behaviour [17], boundary-following [18, 19] and rheotaxis [20].

The self-generation of concentration gradients is typically achieved either through chemical patterning [21], solute advection [22], or geometric effects such as varying particle curvature [23] or through confinement interactions, for instance with a boundary wall [24–26]. The canonical patterned autophoretic microswimmer is the Janus particle [27]; an inert sphere or rod, for instance a polymer, is half-coated in a catalyst for the solute, such as platinum in hydrogen peroxide [28, 29].

Previous theoretical studies on autophoretic motion in three dimensions (3D) have focused on simply connected particle geometries, such as spheres [30] or rods [31]. Theoretical and numerical studies examining the effects of confinement have typically focused upon the prototypical problem of a Janus particle over a plane boundary [24–26], or in the form of multi-particle interactions [32]. In this paper, we explore the phoretic motion of the canonical shape which is not simply connected: the torus. The central hole of the torus provides an example of intrinsic geometric confinement [33], allowing the consequences of this physical effect to be explored, and optimized [8], within an analytical framework. Confinement leads to locally higher concentrations, generating a pumping flow even for uniform surface chemistry. This is similar to the method of generating concentration gradients via changes in surface curvature leading to swimming for axisymmetric shapes where front-back symmetry is broken [23]. This is in contrast to isolated spherical particles, which can only pump flow via chemical patterning (eg Janus particles [5, 31]), interactions with neighbours [30], or solute advection [22].

In this paper, we consider the continuum framework for phoretic motion at zero Péclet number developed by Golestanian et al [5]; for an alternative framework, see [34–36]. Using toroidal coordinates, we derive the analyti-

* t.d.johnson@bham.ac.uk

cal solution for the phoretic torus with axisymmetric boundary conditions in terms of an infinite sum of Legendre polynomials of half-integer order. We consider several cases, with specific solutions validated against 3D regularized boundary element code [37]. We find optimal tori of fixed surface area, an important constraint for controlling reaction rates [38], that either produce the most pumping or maximize swimming speed. In contrast to previous studies [30, 33, 39], these optima do not occur when confinement is maximized (i.e. where the hole is infinitely small).

II. THE AUTOPHORETIC TORUS

A. Continuum framework

We consider the autophoretic motion of a torus \mathcal{S} , with axisymmetric surface chemistry, in the continuum framework [5, 31]. The torus interacts with a solute fuel S . Catalysis at the surface of the torus converts the fuel to a product P , which has a local concentration c and is dissolved in a fluid of dynamic viscosity μ and a density ρ . The torus has surface activity $\mathcal{A}(\mathbf{x})$, such that the flux of product through the surface is

$$-D\mathbf{n} \cdot \nabla c = \mathcal{A}(\mathbf{x}), \quad (1)$$

where \mathbf{n} is the unit normal pointing into the fluid, D denotes the diffusivity of the product, and c is the concentration difference against the far field. If the Péclet number $\text{Pe} = \mathcal{U}\mathcal{R}/D$ is small, with \mathcal{U} and \mathcal{R} being characteristic velocity and length scales of the problem, the concentration c satisfies

$$\nabla^2 c = 0 \quad \text{outside } \mathcal{S}, \quad c \rightarrow 0 \quad \text{as } r \rightarrow \infty, \quad (2)$$

together with the Neumann boundary condition (1), appropriate when the ratio of diffusive to reactive timescales, the Damköhler number, is small [40]. The interaction between \mathcal{S} and the solute can be modelled as giving rise to a slip velocity along the surface

$$\mathbf{u}_s = M(\mathbf{x})(\mathbf{1} - \mathbf{nn}) \cdot \nabla c \quad \text{on } \mathcal{S}, \quad (3)$$

with $M(\mathbf{x})$ the local surface mobility of \mathcal{S} . Neglecting inertial effects, due to typical particle size and flow speeds being small, the flow around the torus is then governed by the Stokes flow equations

$$\mu \nabla^2 \mathbf{u} = \nabla p, \quad (4a)$$

$$\nabla \cdot \mathbf{u} = 0. \quad (4b)$$

For the axisymmetric torus, the swimming velocity is $\mathbf{U} = U\mathbf{e}_z$, which can be obtained by requiring there to be zero net force on \mathcal{S} . Working in the reference frame centered on the torus, the boundary conditions for the Stokes flow problem become

$$\mathbf{u} = \mathbf{u}_s \quad \text{on } \mathcal{S}, \quad \mathbf{u} \sim -U\mathbf{e}_z \quad \text{as } r \rightarrow \infty. \quad (5)$$

Taking \mathcal{A} and M to be typical magnitudes of the surface activity and mobility respectively, we nondimensionalize the problem by setting $\mathcal{A}\mathcal{R}/D$ to be the characteristic size of concentration fluctuations, $M\mathcal{A}/D$ the characteristic size of the slip velocity, and $\mu M\mathcal{A}/(\mathcal{R}D)$ as the characteristic size of the dynamic pressure.

B. Toroidal coordinates

Let (ρ, ϕ, z) be standard cylindrical coordinates. For this problem we introduce toroidal coordinates [41, 42] (ξ, η, ϕ) , which are related to cylindrical coordinates through the transformation

$$\rho = d \frac{\sinh \xi}{\cosh \xi - \cos \eta}, \quad z = d \frac{\sin \eta}{\cosh \xi - \cos \eta}, \quad (6)$$

where $d > 0$, $0 \leq \xi < \infty$ and $0 \leq \eta < 2\pi$. In this coordinate system, shown in Fig. 1, curves of constant ξ correspond to circles in the (ρ, z) plane with radius $a = d/\sinh \xi$, centred at $(b, 0)$, where $b = d \cosh \xi / \sinh \xi$. Rotating by 2π around the z axis, the curves of constant ξ become tori. The scale factors h_i and the unit vectors \mathbf{e}_i are given by

$$h_i \mathbf{e}_i = \frac{\partial \mathbf{x}}{\partial q_i}, \quad \text{so that} \quad h_\xi = h_\eta = \frac{d}{\cosh \xi - \cos \eta}, \quad h_\phi = \frac{d \sinh \xi}{\cosh \xi - \cos \eta}, \quad (7)$$

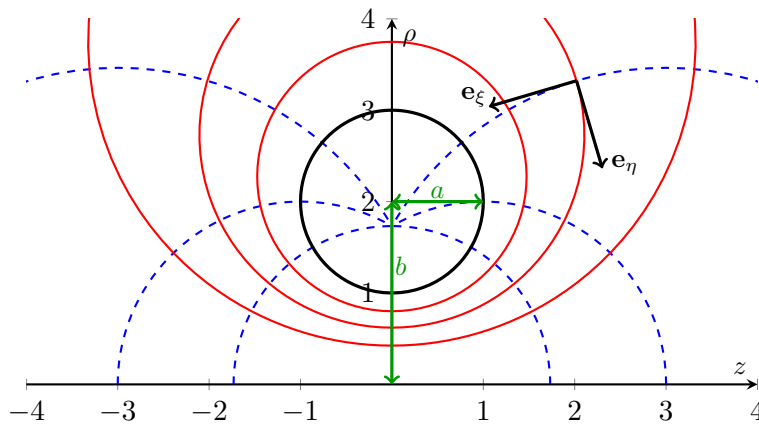


FIG. 1. Toroidal coordinates (redrawn from Ref. [41]) for a torus with $a = 1, b = 2$, with lines of constant ξ (red, solid) and lines of constant η (blue, dashed). The contour $\xi = \xi_0$ represents the boundary of the torus and is shown by the thick black circle. The unit vectors $\mathbf{e}_\xi, \mathbf{e}_\eta$ are shown at $\xi = 0.75, \eta = \pi/6$.

and the unit vectors \mathbf{e}_ξ and \mathbf{e}_η are

$$\mathbf{e}_\xi = \frac{1 - \cosh \xi \cos \eta}{\cosh \xi - \cos \eta} \mathbf{e}_\rho - \frac{\sin \eta \sinh \xi}{\cosh \xi - \cos \eta} \mathbf{e}_z, \quad (8a)$$

$$\mathbf{e}_\eta = -\frac{\sin \eta \sinh \xi}{\cosh \xi - \cos \eta} \mathbf{e}_\rho + \frac{\cosh \xi \cos \eta - 1}{\cosh \xi - \cos \eta} \mathbf{e}_z. \quad (8b)$$

We take the torus \mathcal{S} to be the surface $\xi = \xi_0$, with aspect ratio $s_0 = \cosh \xi_0 = b/a$, then the unit normal pointing into the fluid $\mathbf{n} = -\mathbf{e}_{\xi_0}$, and spatial infinity corresponds to $\xi, \eta \rightarrow 0$. Note that we can relate the toroidal coordinates to the poloidal angle $\theta \in [0, 2\pi)$ on the surface of the torus; a point on the torus' surface is specified by $\rho = b + a \cos \theta$ and $z = a \sin \theta$, so that θ is related to ξ, η through (6) and

$$\tan \theta = \frac{z}{\rho - b}. \quad (9)$$

C. Flow field around a phoretic torus

The tori considered in this work have axisymmetric surface chemistry, and hence the nondimensional surface activity and surface mobility $A = A(\eta)$ and $M = M(\eta)$ respectively are solely functions of η .

1. Product concentration

In the case of fixed-flux, we can think equivalently in terms of solute reducing at the boundary, or product increasing at the boundary, the solutions differing by a minus sign. Here we work in terms of positive product concentrations relative to a zero concentration at infinity. The axisymmetric activity gives rise to $c = c(\xi, \eta)$, and hence Laplace's equation,(2), becomes

$$0 = \frac{\partial}{\partial \xi} \left(\frac{\sinh \xi}{\cosh \xi - \cos \eta} \frac{\partial c}{\partial \xi} \right) + \frac{\partial}{\partial \eta} \left(\frac{\sinh \xi}{\cosh \xi - \cos \eta} \frac{\partial c}{\partial \eta} \right). \quad (10)$$

Let $s = \cosh \xi$, $t = \cos \eta$, and let $P_{m-1/2}, Q_{m-1/2}$ denote Legendre functions of the first and second kind of degree $m - 1/2$ respectively. Then eq. (10) admits a solution, which decays at spatial infinity and is 2π periodic in η , of the form [42]

$$c(\xi, \eta) = \sqrt{s-t} \sum_{n=0}^{\infty} (A_n \cos n\eta + B_n \sin n\eta) P_{n-1/2}(s), \quad (11)$$

where $\sum_{n=0}^{\infty}'$ indicates that the term with $n = 0$ is multiplied by $1/2$. Imposing the Neumann boundary condition (1) then requires

$$\mathbf{e}_\xi \cdot \nabla c = \frac{1}{h_\xi} \frac{\partial c}{\partial \xi} = A(\eta) \quad \text{on } \xi = \xi_0. \quad (12)$$

Using the form of the concentration (11), we can rearrange the above to give

$$\frac{A(\eta)d}{\sinh \xi_0 \sqrt{s_0 - t}} = \sum_{n=0}^{\infty}' (A_n \cos n\eta + B_n \sin n\eta) \left(\frac{1}{2} P_{n-1/2}(s_0) + (s_0 - t) P'_{n-1/2}(s_0) \right), \quad (13a)$$

$$= \sum_{n=0}^{\infty}' (C_n \cos n\eta + D_n \sin n\eta). \quad (13b)$$

The Fourier coefficients (C_n, D_n) can be related to the (A_i, B_i) through standard trigonometric identities. The coefficients A_n and B_n can be calculated numerically after truncating the system.

2. Slip velocity

Once the concentration has been calculated, the slip velocity can be obtained from eqs. (3) and (11) in terms of the nondimensional surface mobility M as

$$\begin{aligned} \mathbf{u}_s &= \frac{M}{a} \frac{\partial c}{\partial \theta} \mathbf{e}_\theta = \frac{M}{h_\eta} \frac{\partial c}{\partial \eta} \mathbf{e}_\eta, \\ &= \frac{M}{d} \left[\frac{1}{2} c(\xi_0, \eta) \sin \eta + (s_0 - \cos \eta)^{3/2} \sum_{n=1}^{\infty} (-n A_n \sin n\eta + n B_n \cos n\eta) P_{n-1/2}(s_0) \right] \mathbf{e}_\eta. \end{aligned} \quad (14)$$

As the A_n are linear in d , the slip velocity depends on the geometry of the system only through the aspect ratio s_0 and not the absolute size of the torus, in an analogous manner to the size independent swimming velocity of spherical Janus particles in the fixed flux limit [31].

3. Stokes streamfunction

The Stokes flow problem for a torus has been solved by Pell and Payne [43] for a fixed torus in uniform flow, and by Leshansky and Kenneth [41] for a torus with slip velocity symmetric about $\eta = \pi$. In this section, we summarize the results and apply them to the case that the slip velocity is given by eq. (14). To identically solve the continuity equation (4b), we introduce the vector potential \mathbf{A} such that $\mathbf{u} = \nabla \times \mathbf{A}$. For axisymmetric flows we may take $\mathbf{A} = \Psi \mathbf{e}_\phi / \rho$, and then the velocity components are given, in cylindrical and toroidal coordinates respectively,

$$u_\rho = -\frac{1}{\rho} \frac{\partial \Psi}{\partial z}, \quad u_z = \frac{1}{\rho} \frac{\partial \Psi}{\partial \rho}, \quad (15a)$$

$$u_\xi = \frac{1}{\rho h_\eta} \frac{\partial \Psi}{\partial \eta}, \quad u_\eta = -\frac{1}{\rho h_\xi} \frac{\partial \Psi}{\partial \xi}. \quad (15b)$$

The stream function Ψ satisfies $L_{-1}^2 \Psi = 0$, where the operator L_k is given by

$$L_k = \frac{\partial^2}{\partial \rho^2} + \frac{\partial^2}{\partial z^2} + \frac{k}{\rho} \frac{\partial}{\partial \rho}. \quad (16)$$

For the boundary conditions on the streamfunction, we ask that the surface $\xi = \xi_0$ be a streamline $\Psi = \chi$, where χ is a constant, and that on the surface there is a slip velocity $\mathbf{u} = u_s(\eta) \mathbf{e}_\eta$ given by eq. (15b). Working in the reference frame where the torus is fixed, we require the background flow at infinity to be uniform with $\Psi \sim -\frac{1}{2} U \rho^2$ as $r \rightarrow \infty$, where U is the swimming velocity of the torus. Writing $\Psi = -\frac{1}{2} U \rho^2 + \psi + \chi \varphi$, the boundary conditions become, as in [41],

$$\psi = \frac{1}{2} U \rho^2, \quad \frac{\partial \psi}{\partial \chi} = U \rho \frac{\partial \rho}{\partial \xi} - \rho h_\xi u_s(\eta), \quad (17a)$$

$$\varphi = 1, \quad \frac{\partial \varphi}{\partial \xi} = 0, \quad (17b)$$

on the surface $\xi = \xi_0$. Setting ψ^k to be solutions to $L_k\psi^k = 0$, we can represent $\psi = \frac{1}{2}\rho^2 (\psi^1 + (r^2 + d^2)\psi^3)$ [43, 44]. We can then solve for ψ^3 and ψ^1 , which decay at infinity and are 2π periodic in η , using separation of variables to get

$$\psi = \frac{1}{2}\rho^2 (s-t)^{1/2} \sum_{n=0}^{\infty} ' (W_n^1(s) \cos n\eta + W_n^2(s) \sin n\eta), \quad (18)$$

where the coefficient functions W_m^i are

$$W_n^1(s) = a_n P_{n-1/2}(s) + c_n s P'_{n-1/2}, \quad (19a)$$

$$W_n^2(s) = b_n P_{n-1/2}(s) + d_n s P'_{n-1/2}. \quad (19b)$$

Making use of Heine's identity [45],

$$\frac{1}{\sqrt{s - \cos \eta}} = \frac{\sqrt{2}}{\pi} Q_{-1/2}(s) + \frac{2\sqrt{2}}{\pi} \sum_{n=1}^{\infty} Q_{n-1/2}(s) \cos n\eta, \quad (20)$$

the boundary conditions (17a) become

$$W_n^1(s_0) = \frac{2\sqrt{2}}{\pi} U Q_{n-1/2}(s_0), \quad \frac{dW_n^1}{ds_0} = U \frac{2\sqrt{2}}{\pi} Q'_{n-1/2}(s_0) - \frac{2E_n}{\sinh^2 \xi_0}, \quad (21a)$$

$$W_n^2(s_0) = 0, \quad \frac{dW_n^2}{ds_0} = -\frac{2F_n}{\sinh^2 \xi_0}, \quad (21b)$$

where the E_n and F_n are the cosine and sine Fourier coefficients of $u_s / (s_0 - t)^{1/2}$, which can be obtained from the expression for the slip velocity (14). The boundary conditions for φ (17b) are exactly as in [41, 43] (given as ψ_1 in the references), whence

$$\varphi = \frac{\rho^2}{d^2} (s-t)^{1/2} \sum_{n=0}^{\infty} ' (e_n P_{n-1/2}(s) + f_n s P'_{n-1/2}(s)) \cos n\eta, \quad (22)$$

with the coefficients f_n and e_n given by

$$f_n s_0 P'_{n-1/2}(s_0) + e_n P_{n-1/2}(s_0) = \frac{3}{\pi\sqrt{2}} Q_{n-1/2}^{-2}(s_0), \quad (23a)$$

$$f_n \frac{d}{ds_0} (s_0 P'_{n-1/2}(s_0)) + e_n P'_{n-1/2}(s_0) = \frac{3}{\pi\sqrt{2}} \frac{d}{ds_0} (Q_{n-1/2}^{-2}(s_0)). \quad (23b)$$

Following Leshansky and Kenneth [41], linearity allows us to split ψ into the contributions from the uniform background flow and the slip velocity, $\psi = U\psi^{(g)} + \psi^{(p)}$, where U is the undetermined non-dimensional swimming velocity. Here $\psi^{(p)}$ is the streamfunction appropriate for a fixed torus with slip velocity u_s , and $\psi^{(g)}$ solves the problem of a torus with no slip velocity in a background flow with $U = 1$. This has the effect that $a_n = U a_n^{(g)} + a_n^{(p)}$ and similarly for other coefficients. The coefficients b_n, d_n depend only on the slip velocity and hence do not pick up contributions from the background flow. The constant χ is found from the requirement that the pressure is single valued, see [41, 43, 44] for details, as

$$\chi = -\frac{d^2 \sum_{n=0}^{\infty} ' (U c_n^{(g)} + c_n^{(p)})}{2 \sum_{n=0}^{\infty} ' f_n} \equiv -\frac{d^2}{2} (U\alpha + \beta). \quad (24)$$

Finally, to determine U , we impose that the force on the torus must vanish. We find the force on the torus, which by symmetry is along the z axis, from

$$\frac{F}{8\pi\mu} = \lim_{r \rightarrow \infty} \frac{r(\psi + \chi\varphi)}{\rho^2}, \quad (25)$$

which is equivalent to evaluating the fraction at $\eta = \xi = 0$. Using the split form of ψ and setting $F = 0$ in (25), we can derive the expression for the swimming velocity of the torus as in [41]

$$U = -\frac{\sum_{n=0}^{\infty} ' \left((n^2 - \frac{1}{4}) (c_n^{(p)} - \beta f_n) + 2 (a_n^{(p)} - \beta e_n) \right)}{\sum_{n=0}^{\infty} ' \left((n^2 - \frac{1}{4}) (c_n^{(g)} - \alpha f_n) + 2 (a_n^{(g)} - \alpha e_n) \right)}. \quad (26)$$

We now apply the solution to analyse special cases of particular interest.

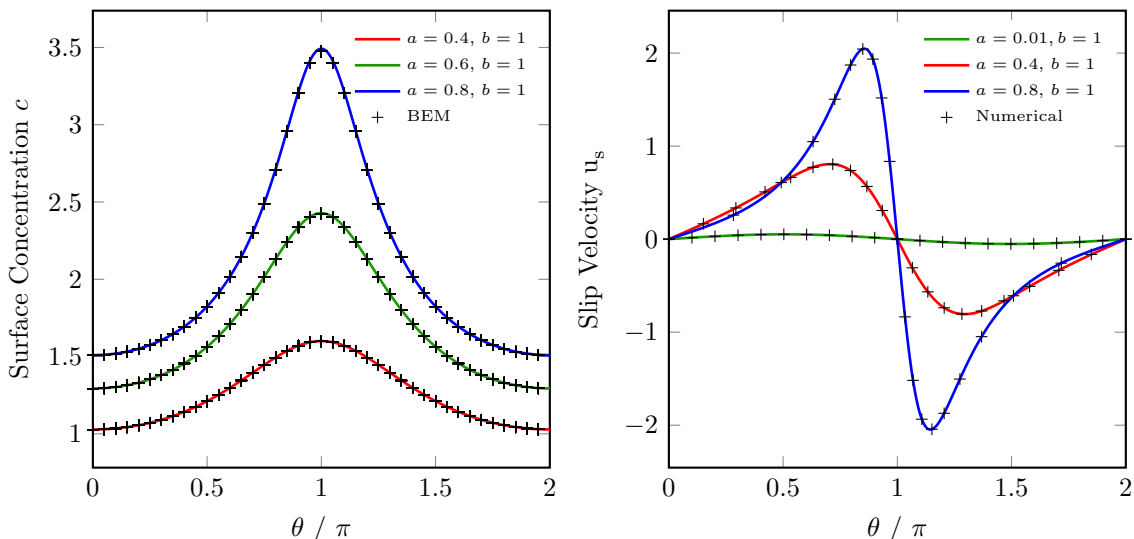


FIG. 2. Validation of the series solution. Left: Surface concentration as a function of the poloidal angle θ , with the analytical series solution (lines) compared against a numerical solution (crosses) computed with a 3D boundary element method [37]. Right: Slip velocity as a function of θ , with the series solution (lines) compared against results obtained from numerically differentiating the validated series solution for the concentration (crosses).

III. RESULTS

A. The optimal uniform toroidal pump

First, we consider the chemically-uniform case where both activity A and mobility M are constants, ± 1 . We can use Heine's identity (20) in the expressions for the concentration coefficients (13a) to set $B_n = D_n = 0$, and then the A_n are determined through

$$\frac{2\sqrt{2}}{\pi}Q_{-1/2}(s_0) = A_0 \left[\frac{1}{2}P_{-1/2}(s_0) + s_0 P'_{-1/2}(s_0) \right] - A_1 P'_{1/2}(s_0), \quad (27a)$$

$$\begin{aligned} \frac{2\sqrt{2}}{\pi}Q_{n-1/2}(s_0) &= A_n \left[\frac{1}{2}P_{n-1/2}(s_0) + s_0 P'_{n-1/2}(s_0) \right] \\ &\quad - \frac{1}{2} \left[A_{n+1} P'_{n+1/2}(s_0) + A_{n-1} P'_{n-3/2}(s_0) \right]. \end{aligned} \quad (27b)$$

Truncating the system (27a, 27b) at an appropriately chosen n enables numerical computation of the A_i . Throughout this study we take between $n = 45$ and $n = 5$ coefficients for aspect ratios in the range $s_0 = 1.1$ and $s_0 = 30$, similar to the numbers used by Leshansky and Kenneth [41]. To check the numerical accuracy, we compare the surface concentration calculated from the analytical solution against the surface concentration obtained from a 3D regularized boundary element method [37]. The comparison (Fig. 2, left) shows the surface concentrations to be in good agreement with a maximal percentage difference of less than 0.5% for $a = 0.8$ and $b = 1$.

In contrast to isolated spherical particles, where a uniform surface chemistry is unable to drive flow [30, 31], a uniform phoretic torus generates a pumping flow field. When the torus releases product, confinement causes this product to build-up in the central hole (see Figs. 2 and 3, left), and the resulting concentration gradients give rise to the slip velocities on the surface (see Fig. 2, right) which drive the overall flow. The confining effect becomes more pronounced in the limit where the central hole shrinks and the aspect ratio $s_0 = b/a \rightarrow 1$. In this limit, the concentration becomes increasingly localized in the central hole, leading to large peaks in the slip velocity moving closer to either side of $\theta = \pi$ as the differences in the confining effect between neighbouring points becomes greater.

However, on the outer edge of the torus, the largest slip velocities do not occur in the limit where the central hole vanishes (Fig. 2, right). Since the strength of pumping will depend in some sense on an integral of slip velocities over the toroidal surface, this result suggests that for fixed surface area, there may be a non-trivial optimal pump.

We test this notion by calculating the flow in the bulk of the fluid via the streamfunction Ψ . For uniform surface chemistry, symmetry prevents the system from swimming, thus $U = 0$. Additionally we require that Ψ is antisymmetric in η around $\eta = \pi$, which forces $\chi = 0$, and hence $\Psi = \psi$ with $W_n^1(s) = 0$. The Fourier coefficients F_n in (21b) can

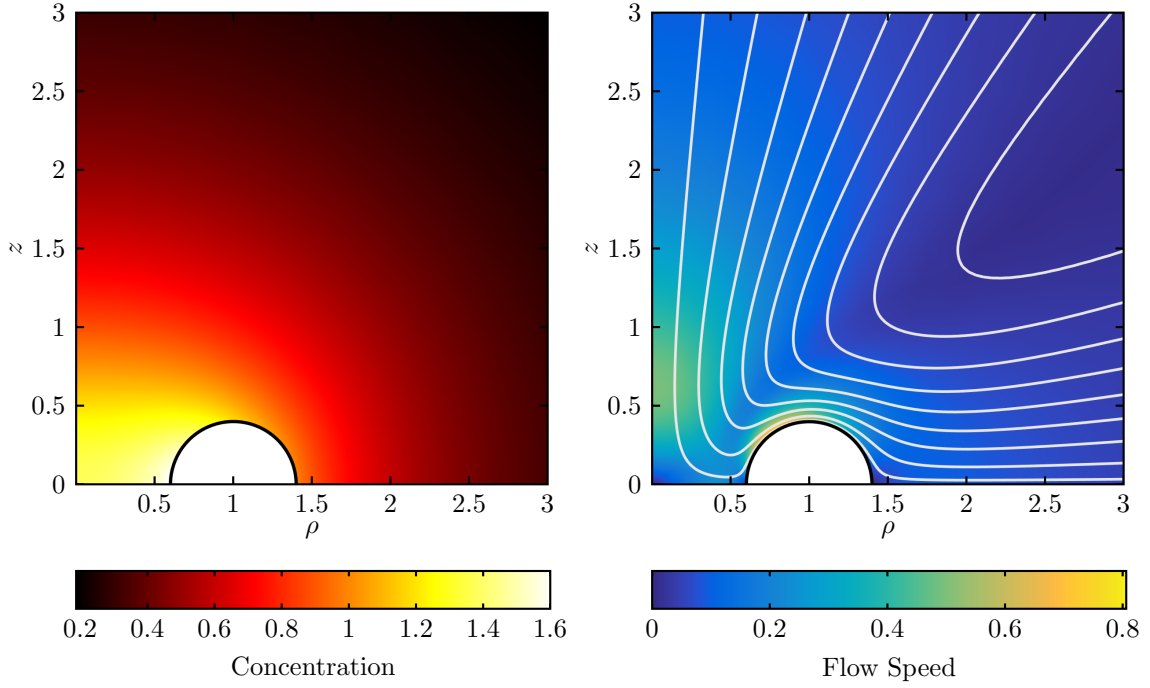


FIG. 3. Left: Product concentration around uniform torus for $a = 0.4$, $b = 1$ and constant surface activity $A = +1$, computed with the analytical series solution. Right: Flow speed around torus with $a = 0.4$, $b = 1$ and $A = M = +1$, computed with the analytical series solution; flow streamlines shown in white.

be found from the slip velocity (14) in terms of the concentration coefficients A_i as

$$F_n = \frac{M}{d} \left(-nA_n s_0 P_{n-1/2}(s_0) + \left(\frac{n}{2} - \frac{1}{4}\right) A_{n-1} P_{n-3/2}(s_0) + \left(\frac{n}{2} + \frac{1}{4}\right) A_{n+1} P_{n+1/2}(s_0) \right). \quad (28)$$

Using equations (15b), these coefficients then allow us to compute the flow. The right of Fig. 3 shows the flow speed $u = (u_\xi^2 + u_\eta^2)^{1/2}$ and corresponding streamlines. When $AM = 1$, the fluid comes in along the ρ direction and is pushed out again along the z direction (if $AM = -1$ the flow direction is reversed).

By symmetry the pumping torus is force-free, thus we expect the far-field flow to behave like a stresslet, i.e. the solution to Stokes flow driven by a point stress [46]. As such, we predict flow decays like $u \propto 1/r^2$ away from the torus. Considering the flow speed along the ρ axis, we should therefore see

$$|u|_{z=0} \sim \frac{k}{\rho^2}. \quad (29)$$

Along $z = 0$, we have $\eta = 0$ and $|\mathbf{u}| = |u_\xi|$. From eqs. (18) and (15b) we find that along $\eta = 0$

$$u_\xi = \frac{1}{2} \sinh \xi (s-1)^{1/2} \sum_{n=1}^{\infty} n W_n^2(s). \quad (30)$$

Using $\sinh \xi = \sqrt{(s-1)(s+1)}$, $(s-1) \sim 2\frac{d^2}{\rho^2}$ along $\eta = 0$ as $s \rightarrow 1$, and the asymptotic forms of the toroidal harmonics [47] as $s \rightarrow 1$ in (30) we find that

$$k = \left| \sqrt{2} d^2 \sum_{n=1}^{\infty} n \left(b_n + \frac{1}{2} d_n \left(n^2 - \frac{1}{4} \right) \right) \right|, \quad (31)$$

giving the strength of the pumping k for a given torus in terms of the stream function coefficients b_n and d_n . We can use this expression to optimize the torus to maximize the pumping.

The area of the active surface on the torus governs the net flux of product into the solution [38]. Fixing the surface area $A_s = 4\pi^2 ab$, we still have the freedom to vary the aspect ratio of the torus $s_0 = b/a = \cosh \xi_0$. Measuring the

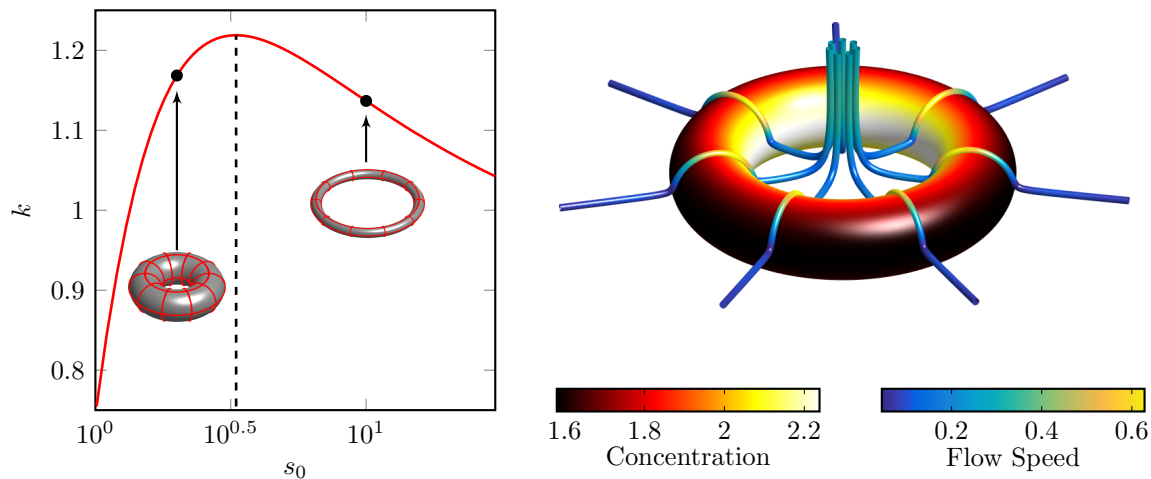


FIG. 4. Left: Decay coefficient k as a function of aspect ratio s_0 for fixed surface area $A_s = 4\pi^2$, as calculated by the series (31). Tori with $s_0 = 2$ and $s_0 = 10$ are shown for comparison. Right: The concentration and flow streamlines of the optimal uniform torus with $A_s = 4\pi^2$, as calculated with the analytical series solution.

pumping strength of the uniform torus through $k(s_0)$ of (29), we seek the optimal aspect ratio which maximizes the pumping. From the left of Fig. 4, we see that there is a peak in the stresslet strength with an optimal aspect ratio at $s_0 = 3.31$. The corresponding optimal torus is shown on the right of Fig. 4, notice in particular that the optimum interestingly occurs for a torus with a central hole, so that pumping is not maximized for the aspect ratio which maximizes geometric confinement.

B. Optimal smooth-activity Janus torus

We consider next a smoothed approximation to a Janus torus. We take the differentiable surface activity of the form

$$A = \frac{1}{2}(1 + \sin \theta) = \frac{1}{2} \left(1 + \frac{\sin \eta \sinh \xi_0}{\cosh \xi_0 - \cos \eta} \right), \quad (32)$$

while the surface mobility is kept constant $M = \pm 1$ [48]. Such smooth activity functions are numerically convenient, and may be employed [25] for studies of spherical Janus particles, which in reality have discontinuities in the surface activity at the boundary of the active and inert portions of their surfaces. The top-bottom asymmetry in the surface activity produces asymmetric concentration gradients and slip velocities (see Fig. 5) which allow the torus to have a nonzero swimming velocity. For $M = 1$, swimming occurs along the negative z direction ($M = -1$ reverses flow and swimming directions).

The confinement and changes in the surface activity lead to two areas on the surface of the torus where there are significant slip velocities, visible on the right of Fig. 5. The first area of large slip velocities occurs on lower half of the central hole, due to the decrease in the value of the activity, while the second occurs towards the outer edge of the torus as a result of the increased freedom for the product to diffuse. As before we validate the accuracy of these solutions by comparing the results obtained by truncating the analytical expressions against the boundary element method, the details of which are described in Ref. [37]. Over the range $1.1 \leq s_0 \leq 10$, with fixed $A_s = 4\pi^2$, we obtain percentage differences between the concentrations calculated using the two methods of at most than 1.1% for $s_0 = 1.1$. However, this error is likely attributable to the difficulty of modelling small aspect ratio tori accurately with the boundary element method; larger aspect ratios, which are easier to model with boundary elements, give smaller percentage differences; for example, for $s_0 = 2.81$ the difference calculated was less than 0.03%.

As in §III B, we compute $|U|$ as we vary the aspect ratio s_0 (Fig. 6, left). There is a peak at $s_0 = 2.81$, with swimming speed $|U| = 0.2518$, before the swimming velocity appears to tend towards an asymptote for larger s_0 . In the large s_0 limit, there is no self-interaction between the opposing ends of the torus. The swimming speed being independent of the torus shape in this limit is similar to the result for spherical Janus particles, whose swimming speed is independent of their size in this classical phoretic framework [31].

The optimal smooth-activity torus, shown on the right of Fig. 6, has a smaller aspect ratio $s_0 = 2.81$ than the optimal toroidal pump $s_0 = 3.31$. This difference arises because the swimming optimum arises from the balance of

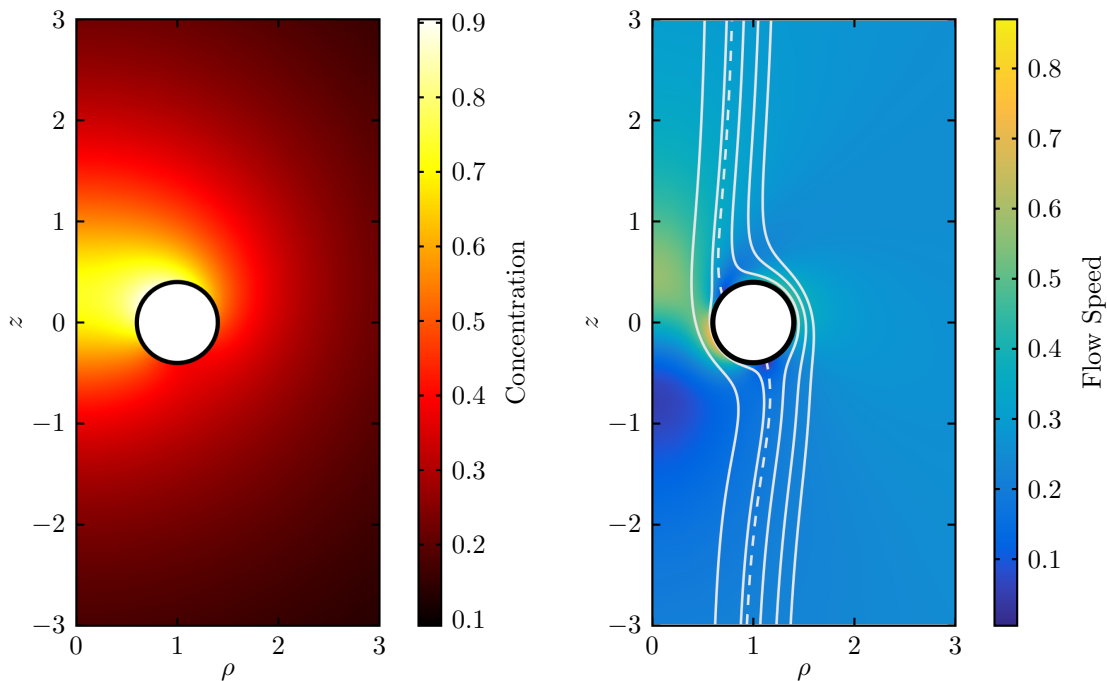


FIG. 5. Left: Concentration around the smooth-activity Janus torus with $a = 0.4$ and $b = 1$ computed from the analytical series solution. Right: Flow speed around the smooth-activity Janus torus with $a = 0.4$ and $b = 1$. Streamlines in the body frame in white, with dashed streamlines correspond to dividing streamlines $\psi = \chi$.

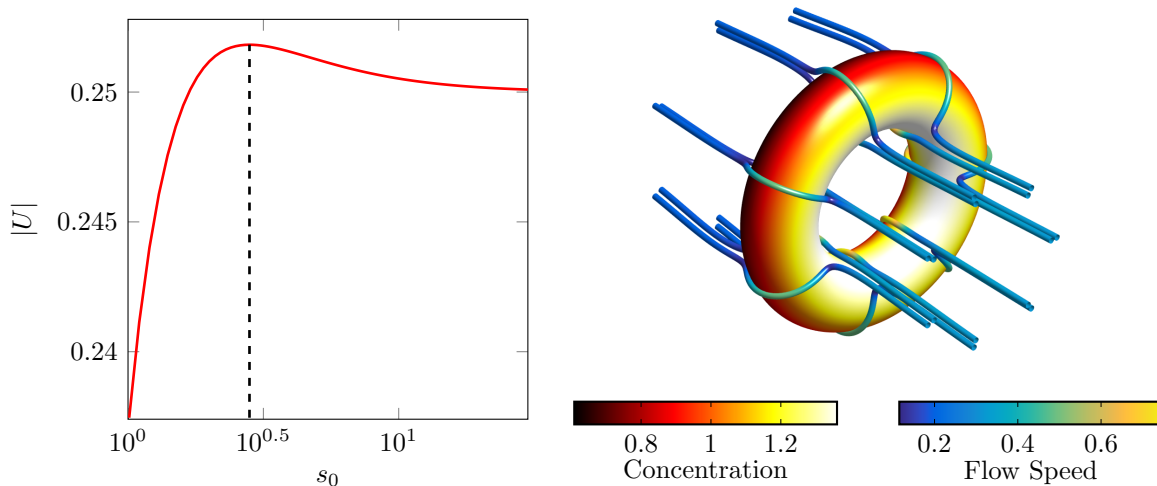


FIG. 6. Left: Swimming speed $|U|$ of the smooth-activity Janus torus as a function of s_0 . Right: The optimal smooth-activity Janus torus with surface concentration and streamlines in the body frame. Computed with the analytical series solution.

two physical effects; maximising surface chemical gradients/slip flow, as with the pump, and minimising drag via hydrodynamic interactions. The proximity of the opposing side of the torus reduces drag by pulling its neighbouring segments along, an effect which is also observed for groups of sedimenting spheres [49]. Thus, the swimming optimum has a smaller central hole than the pump; suboptimal slip generation is balanced by reduced drag in this fatter torus.

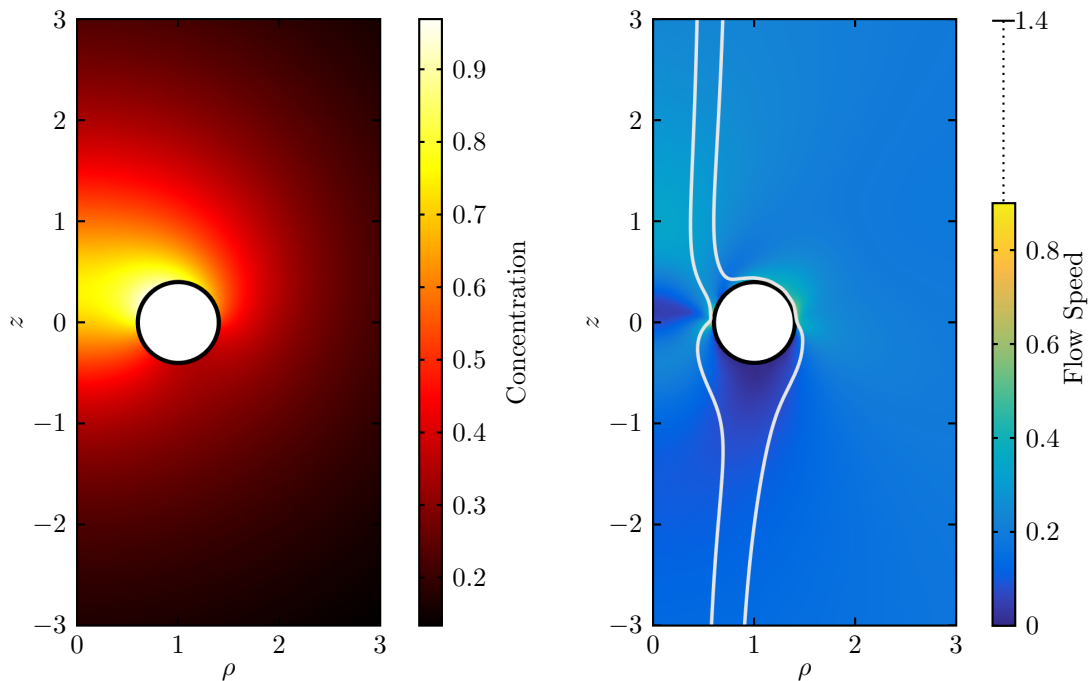


FIG. 7. Left: Concentration around a Janus torus with $a = 0.4$ and $b = 1$. Right: Flow speed around Janus torus with $a = 0.4$ and $b = 1$. Computed with the analytical series solution.

C. Optimal Janus torus

Finally, we consider a Janus torus, with both the surface activity and surface mobility having a step-discontinuity at $\theta = \pi$, given by

$$A = M = \begin{cases} 1 & \text{if } \theta \in (0, \pi), \\ 0 & \text{if } \theta \in (\pi, 2\pi). \end{cases} \quad (33)$$

The set of linear equations for the concentration coefficients (11) becomes ill conditioned when attempting to solve for a large number of coefficients. This makes it difficult to accurately resolve the step discontinuities in the activity and mobility using the series solution. However, due to the dissipative nature of Stokes flow, the wiggles in the boundary condition are smoothed out quickly in the fluid, and the swimming velocity is dependent upon an integral of the boundary slip. Thus we expect the error introduced by the low number of coefficients to be small, and we check the error introduced by comparing the computed results against the boundary element method [37]. The swimming speeds calculated using the two methods have percentage differences of at most 3%.

The concentration around the Janus torus (Fig. 7, left) is similar to concentration found for the first-mode approximation in §III B, with the product slightly more evenly distributed around the smooth-activity torus. These differences can produce larger changes in the slip velocity, and thus in the swimming speed. Away from the surface of the torus the flow fields (Fig. 7, right) calculated using the two methods described are in good agreement. Notice that the colorbar has been truncated at $u = 0.9$, highlighting the structure of the flow field. The most prominent difference, compared with the previously considered torus, is that the area of large surface slip velocities on the lower half of the central hole in Fig. 5 no longer appears for the Janus torus with discontinuous mobility. We again aim to determine the optimal aspect ratio which maximizes the swimming speed of the Janus torus. The green line on Fig. 8 shows the swimming speed of the Janus torus with nonuniform mobility (33). There is a pronounced peak at $s_0 = 1.58$, which corresponds to a torus with a smaller central hole than found for the first-mode smooth-activity Janus torus, shown as the red line.

To determine whether this difference is solely due to the change in mobility or whether it is also affected by the surface activity, we repeat the calculation for a Janus torus with uniform mobility $M = 1$, shown as the blue line on Fig. 8. Whilst perhaps not experimentally relevant, the uniform mobility case has been considered in previous studies [24, 48] and provides an indication of the behaviour of tori with intermediate non-zero mobilities on the inert cap. For the Janus torus with uniform mobility, the optimal swimming speed is achieved for $s_0 = 2.01$, for

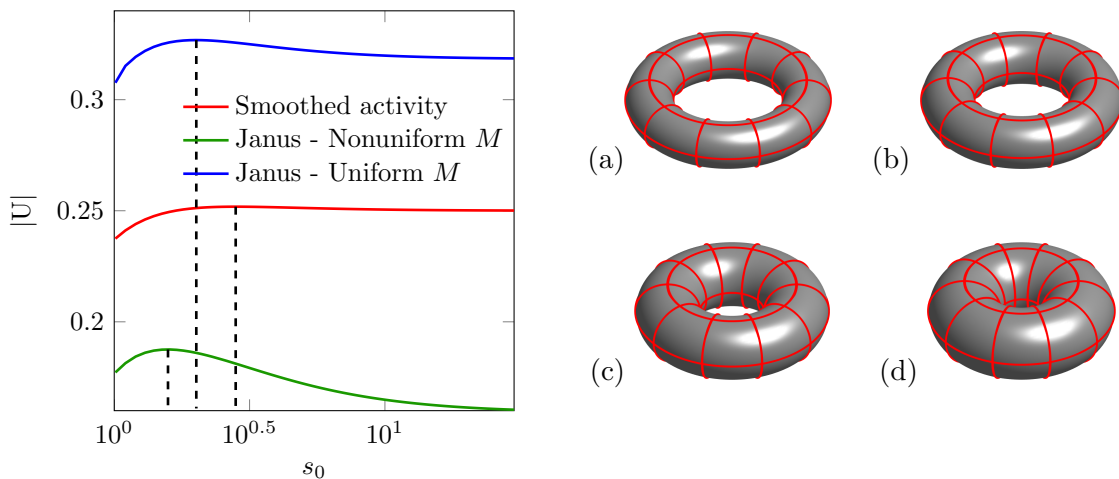


FIG. 8. Left: Swimming speed $|U|$ of Janus torus with surface chemistry given by Eq. (33), computed with the analytical series solution. Right: Plots of the optimal tori: (a) Uniform pump, (b) smooth-activity Janus torus, (c) uniform mobility Janus torus, (d) nonuniform mobility Janus torus.

a swimming speed $|U| = 0.3268$, greater than for the smooth-activity Janus torus. Additionally, the peak in the swimming velocity is much sharper than for the first-mode smooth-activity Janus torus. Notably, in the fixed-flux limit which we consider, the swimming speed of a spherical Janus particle is independent of size with $|U| = 0.25$ for uniform mobility [31], so that the optimal Janus torus is 31% faster.

For the Janus torus, the swimming speed in the case of nonuniform mobility is lower than for uniform mobility, and there is a much sharper peak around the optimum than for the other cases. This is because concentration gradients after $\theta = \pi$ cannot contribute to the swimming velocity. The product concentration (Fig. 7, left) shows that there are large surface concentration gradients on the inside of the torus, around $\theta = \pi$, which do not all contribute to U . The position and extent of these concentration gradients depend on s_0 , giving rise to the sharper peak for the nonuniform mobility.

IV. DISCUSSION

In this paper we computed the analytical solution for the autophoretic motion of an axisymmetric torus in a neutral solute, in the purely diffusive limit and following the continuum framework of Golestanian et al [5]. Using separation of variables in toroidal coordinates, we solved for the product concentration outside of the torus in the case of axisymmetric surface activity. In the central hole, geometric confinement leads to locally higher product concentrations, creating surface concentration gradients that drive slip flow even in the absence of chemical patterning. Upon optimizing swimming and pumping with respect to fixed surface area, we found that maximal confinement is not optimal, demonstrating a qualitative difference to the optima of other autophoretic systems driven purely by geometric confinement [33, 39].

For the chemically uniform torus (i.e. $A, M = \pm 1$) symmetry prevents swimming, but concentration gradients from the central hole generate a pumping flow. We characterized this pumping flow by the strength of the resulting stresslet singularity. Fixing the surface area, we varied the aspect ratio s_0 ; for vanishing central holes, $s_0 \rightarrow 1$, the concentration is very large around $\theta = \pi$, however these large local concentrations do not necessarily lead to large concentration gradients across the torus surface. Meanwhile, for large s_0 , the distance between opposing ends of the torus means confinement weakens, correspondingly there are smaller concentration variations over the surface of the torus. These effects lead to an optimal torus with nonvanishing central hole at $s_0 = 3.31$, which maximizes the strength of the pumping flow, and yields the stresslet with the highest coefficient k .

We next considered nonuniform tori where the up-down symmetry of the system is broken, resulting in swimming. We examined a smoothed approximation to the activity of a Janus torus, as such first-mode regularizations of Janus particles are used in the study of spherical Janus particles [25], and then we compared it against a full Janus torus where we took both the surface activity and mobility to have step discontinuities at $\theta = 0$ and π . In maximising the swimming velocity of the nonuniform tori with respect to fixed surface area, we found (Fig. 8) that (b) the optimal smoothed-activity torus, has a larger aspect ratio than the optimum for the full Janus torus with the same uniform

mobility, (c). The optimal swimmers, (b), (c), and (d), all have smaller aspect ratios than (a) the optimal phoretic pump; unlike the pump, swimmers must not only maximize surface concentration gradients, but also minimize drag. The smaller aspect ratios result from the balance of these two effects.

While our study focused on neutral solutes and self-diffusiophoresis, if suitably modified the results may be applied to other phoretic mechanisms. For instance, the auto-thermophoretic torus may be studied provided that both the mechanism of heating is axisymmetric, and additionally the interior problem of heat conduction through the torus is solved. The slip-velocity is then the gradient of the temperature field at the torus surface [50], and the flow solution proceeds as before. For electrophoresis, the situation is more complex as in general it also involves charge transport through the material; slip velocity would then be proportional to the electric field on the torus surface [51], with activity corresponding to electrical current injected into the flow at the surface [31].

The torus is arguably the simplest system that naturally exhibits geometric confinement, an important property that can influence the motion of diffusiophoretic particles leading to physical effects such as boundary steering [18, 19] and dynamic self assembly [15]. Our results provide a means of probing confinement effects analytically, demonstrating key differences between pumps and swimmers.

ACKNOWLEDGMENTS

This work was undertaken as part of EPSRC-funded UROP project. EL is supported in part by the European Union through a Marie Curie CIG grant and an ERC Consolidator grant. TDM-J is supported by a Royal Commission for the Exhibition of 1851 Research Fellowship. The authors are thankful to Sébastien Michelin for fruitful discussions, and to the anonymous referees for useful feedback.

-
- [1] J. L. Anderson and D. C. Prieve. Diffusiophoresis caused by gradients of strongly adsorbing solutes. *Langmuir*, 7:403–406, 1991.
 - [2] A. S. Khair. Diffusiophoresis of colloidal particles in neutral solute gradients at finite pécelet number. *J. Fluid Mech.*, 731:64–94, 2013.
 - [3] H.-R. Jiang, N. Yoshinaga, and M. Sano. Active motion of a Janus particle by self-thermophoresis in a defocused laser beam. *Phys. Rev. Lett.*, 105:268302, 2010.
 - [4] T. Bickel, A. Majee, and A. Würger. Flow pattern in the vicinity of self-propelling hot janus particles. *Phys. Rev. E*, 88:012301, 2013.
 - [5] R. Golestanian, T. B. Liverpool, and A. Ajdari. Propulsion of a molecular machine by asymmetric distribution of reaction products. *Phys. Rev. Lett.*, 94(22):220801, 2005.
 - [6] B. J. Nelson, I. K. Kaliakatsos, and J. J. Abbott. Microrobots for minimally invasive medicine. *Annu. Rev. Biomed. Eng.*, 12(1):55–85, 2010.
 - [7] C. Maggi, J. Simmchen, F. Saglimbeni, J. Katuri, M. Dipalo, F. De Angelis, S. Sanchez, and R. Di Leonardo. Self-assembly of micromachining systems powered by janus micromotors. *Small*, 12(4):446–451, 2016.
 - [8] M. N. Popescu, M. Tasinkevych, and S. Dietrich. Pulling and pushing a cargo with a catalytically active carrier. *Eur. Phys. Lett.*, 95:28004, 2011.
 - [9] L. Baraban, M. Tasinkevych, M. N. Popescu, S. Sanchez, S. Dietrich, and O. G. Schmidt. Transport of cargo by catalytic janus micro-motors. *Soft Matter*, 8(1):48–52, 2012.
 - [10] S. Ebbens, D. A. Gregory, G. Dunderdale, J. R. Howse, Y. Ibrahim, T. B. Liverpool, and R. Golestanian. Electrokinetic effects in catalytic platinum-insulator janus swimmers. *Eur. Phys. Lett.*, 106:58003, 2014.
 - [11] A. Brown and W. Poon. Ionic effects in self-propelled Pt-coated Janus swimmers. *Soft Matter*, 10:4016–4027, 2014.
 - [12] M. N. Popescu, S. Dietrich, M. Tasinkevych, and J. Ralston. Phoretic motion of spheroidal particles due to self-generated solute gradients. *Eur. Phys. J. E*, 31:351–367, 2010.
 - [13] N. Sharifi-Mood, A. Mozaffari, and U. M. Córdoba-Figueroa. Pair interaction of catalytically active colloids: from assembly to escape. *J. Fluid Mech.*, 798:910–954, 007 2016.
 - [14] J. Palacci, S. Sacanna, A. P. Steinberg, D. J. Pine, and P. M. Chaikin. Living crystals of light-activated colloidal surfers. *Science*, 339:936–940, 2013.
 - [15] M. S. Davies Wykes, J. Palacci, T. Adachi, L. Ristroph, X. Zhong, M. D. Ward, J. Zhang, and M. J. Shelley. Dynamic self-assembly of microscale rotors and swimmers. *Soft Matter*, 12(20):4584–4589, 2016.
 - [16] I. Buttinoni, J. Bialké, F. Kümmel, H. Löwen, C. Bechinger, and T. Speck. Dynamical clustering and phase separation in suspensions of self-propelled colloidal particles. *Phys. Rev. Lett.*, 110(23):238301, 2013.
 - [17] S. Thutupalli, R. Seemann, and S. Herminghaus. Swarming behavior of simple model squirmers. *New J. Phys.*, 13:073021, 2011.
 - [18] S. Das, A. Garg, A. I. Campbell, J. Howse, A. Sen, D. Velegol, R. Golestanian, and S. J. Ebbens. Boundaries can steer active janus spheres. *Nature Comms*, 6, 2015.

- [19] J. Simmchen, J. Katuri, W. E. Uspal, M. N. Popescu, M. Tasinkevych, and S. Sánchez. Topographical pathways guide chemical microswimmers. *Nature Commun.*, 7, 2016.
- [20] W. E. Uspal, M. N. Popescu, S. Dietrich, and M. Tasinkevych. Rheotaxis of spherical active particles near a planar wall. *Soft matter*, 11(33):6613–6632, 2015.
- [21] W. F. Paxton, K. C. Kistler, C. C. Olmeda, A. Sen, S. K. St. Angelo, Y. Cao, T. E. Mallouk, P. E. Lammert, and V. H. Crespi. Catalytic Nanomotors: Autonomous Movement of Striped Nanorods. *J. Am. Chem. Soc.*, 126(41):13424–13431, 2004.
- [22] S. Michelin, E. Lauga, and D. Bartolo. Spontaneous autophoretic motion of isotropic particles. *Phys. Fluids*, 25(6):061701, 2013.
- [23] S. Shklyaev, J. F. Brady, and U. M. Córdova-Figueroa. Non-spherical osmotic motor: chemical sailing. *J. Fluid Mech.*, 748:488–520, 2014.
- [24] W. E. Uspal, M. N. Popescu, S. Dietrich, and M. Tasinkevych. Self-propulsion of a catalytically active particle near a planar wall: from reflection to sliding and hovering. *Soft Matter*, 11(3):434–438, 2015.
- [25] Y. Ibrahim and T. B. Liverpool. The dynamics of a self-phoretic janus swimmer near a wall. *Euro. Phys. Lett.*, 111(4):48008, 2015.
- [26] A. Mozaffari, N. Sharifi-Mood, J. Koplik, and C. Maldarelli. Self-diffusiophoretic colloidal propulsion near a solid boundary. *Phys. Fluids*, 28(5):053107, 2016.
- [27] A. Walther and A. H. E. Müller. Janus particles. *Soft Matter*, 4(4):663–668, 2008.
- [28] J. R. Howse, R. A. L. Jones, A. J. Ryan, T. Gough, R. Vafabakhsh, and R. Golestanian. Self-Motile Colloidal Particles: From Directed Propulsion to Random Walk. *Phys. Rev. Lett.*, 99(4):048102, 2007.
- [29] S. J. Ebbens and J. R. Howse. Direct observation of the direction of motion for spherical catalytic swimmers. *Langmuir*, 27:12293–12296, 2011.
- [30] S. Michelin and E. Lauga. Autophoretic locomotion from geometric asymmetry. *Euro. Phys. J. E*, 38(2):1–16, 2015.
- [31] R. Golestanian, T. B. Liverpool, and A. Ajdari. Designing phoretic micro- and nano-swimmers. *New J. Phys.*, 9(5):126, 2007.
- [32] S. Thakur and R. Kapral. Collective dynamics of self-propelled sphere-dimer motors. *Phys. Rev. E*, 85:026121, Feb 2012.
- [33] S. Michelin, T. D. Montenegro-Johnson, G. De Canio, N. Lobato-Dauzier, and E. Lauga. Geometric pumping in autophoretic channels. *Soft Matter*, 11(29):5804–5811, 2015.
- [34] U. M. Córdova-Figueroa and J. F. Brady. Osmotic Propulsion: The Osmotic Motor. *Phys. Rev. Lett.*, 100(15):158303, 2008.
- [35] J. F. Brady. Particle motion driven by solute gradients with application to autonomous motion: continuum and colloidal perspectives. *J. Fluid Mech.*, 667:216–259, 2011.
- [36] U. M. Córdova-Figueroa, J. F. Brady, and S. Shklyaev. Osmotic propulsion of colloidal particles via constant surface flux. *Soft Matter*, 9:6382–6390, 2013.
- [37] T. D. Montenegro-Johnson, S. Michelin, and E. Lauga. A regularised singularity approach to phoretic problems. *Euro. Phys. J. E*, 38(12):1–7, 2015.
- [38] T. D. Montenegro-Johnson and E. Lauga. The other optimal Stokes drag profile. *J. Fluid Mech.*, 762:R5, 2015.
- [39] M. Lisicki, S. Michelin, and E. Lauga. Phoretic flow induced by asymmetric confinement. *J. Fluid Mech.*, 799:R5, 2016.
- [40] S. Michelin and E. Lauga. Phoretic self-propulsion at finite pécelet numbers. *J. Fluid Mech.*, 747:572–604, 2014.
- [41] A. M. Leshansky and O. Kenneth. Surface tank treading: Propulsion of purcells toroidal swimmer. *Phys. Fluids*, 20(6):063104, 2008.
- [42] P. Moon and D. E. Spencer. *Field Theory Handbook*. Springer-Verlag, Berlin, 1961.
- [43] W. H. Pell and L. E. Payne. On stokes flow about a torus. *Mathematika*, 7(01):78–92, 1960.
- [44] L. E. Payne and W. H. Pell. The stokes flow problem for a class of axially symmetric bodies. *J. Fluid Mech.*, 7, 1960.
- [45] E. Heine. *Handbuch der Kugelfunctionen*. G. Reimer, Berlin, 1861.
- [46] G. K. Batchelor. The stress system in a suspension of force-free particles. *J. Fluid Mech.*, 41(03):545–570, 1970.
- [47] M. Andrews. Alternative separation of laplace’s equation in toroidal coordinates and its application to electrostatics. *J. Electrostat.*, 64(10):664–672, 2006.
- [48] A. Nourhani and P. E. Lammert. Geometrical performance of self-phoretic colloids and microswimmers. *Phys. Rev. Lett.*, 116(17):178302, 2016.
- [49] K. O. L. F. Jayaweera, B. J. Mason, and G. W. Slack. The behaviour of clusters of spheres falling in a viscous fluid part 1. experiment. *J. Fluid Mech.*, 20(01):121–128, 1964.
- [50] K. Kroy, D. Chakraborty, and F. Cichos. Hot microswimmers. *Euro. Phys. J. Spec. Top.*, 225(11-12):2207–2225, 2016.
- [51] J. L. Anderson. Colloid transport by interfacial forces. *Ann. Rev. Fluid Mech.*, 21(1):61–99, 1989.